SCIENTIFIC REPORTS

OPEN

SUBJECT AREAS:
COLLOIDS
NANOPARTICLES
ORGANIC-INORGANIC NANOSTRUCTURES

Received
26 March 2014

Accepted
18 June 2014

Published
7 July 2014

Correspondence and requests for materials should be addressed to C.C.H. (cchuang-ym@ym.edu.tw; huang.chihchia@gmail.com)

* These authors contributed equally to this work.

One-step shell polymerization of inorganic nanoparticles and their applications in SERS/nonlinear optical imaging, drug delivery, and catalysis

Tzu-Ming Liu[1]*, Jiashing Yu[2]*, C. Allen Chang[3,4,5], Arthur Chiou[4,5], Huihua Kenny Chiang[4,5,6], Yu-Chun Chuang[7], Cheng-Han Wu[1], Che-Hao Hsu[2], Po-An Chen[4] & Chih-Chia Huang[4,5,8]

[1]Institute of Biomedical Engineering and Molecular Imaging Center, National Taiwan University, Taipei, 106, Taiwan, [2]Department of Chemical Engineering, National Taiwan University, Taipei, 106, Taiwan, [3]Department of Biomedical Imaging and Radiological Sciences National Yang-Ming University, Taipei, 112, Taiwan, [4]Institute of Biophotonics, National Yang-Ming University, Taipei, 112, Taiwan, [5]Biophotonics and Molecular Imaging Research Center (BMIRC), National Yang-Ming University, Taipei, 112, Taiwan, [6]Institute of Biomedical Engineering, National Yang-Ming University, Taipei, 112, Taiwan, [7]National Synchrotron Radiation Research Center, Hsinchu, 300, Taiwan, [8]Department of Applied Chemistry, National University of Kaohsiung, Kaohsiung, 811, Taiwan.

Surface functionalized nanoparticles have found their applications in several fields including biophotonics, nanobiomedicine, biosensing, drug delivery, and catalysis. Quite often, the nanoparticle surfaces must be post-coated with organic or inorganic layers during the synthesis before use. This work reports a generally one-pot synthesis method for the preparation of various inorganic-organic core-shell nanostructures (Au@polymer, Ag@polymer, Cu@polymer, Fe_3O_4@polymer, and TiO_2@polymer), which led to new optical, magnetic, and catalytic applications. This green synthesis involved reacting inorganic precursors and poly(styrene-*alt*-maleic acid). The polystyrene blocks separated from the external aqueous environment acting as a hydrophobic depot for aromatic drugs and thus illustrated the integration of functional nanoobjects for drug delivery. Among these nanocomposites, the Au@polymer nanoparticles with good biocompatibility exhibited shell-dependent signal enhancement in the surface plasmon resonance shift, nonlinear fluorescence, and surface-enhanced Raman scattering properties. These unique optical properties were used for dual-modality imaging on the delivery of the aromatic photosensitizer for photodynamic therapy to HeLa cells.

Over the past few decades, nanomaterials have been shown to exhibit various optical and magnetic properties and have been integrated with drug carriers for multifunctional applications in biophotonics and nanobiomedicine[1–5]. Although there are many known strategies to fabricate nanoparticles, the challenge still remains in developing one general method for synthesizing the different types of inorganic nanoparticles while controlling particle size, shape, and composition. The current synthesis reaction keeps complex procedures and undesired toxic reagents at minimum.

Specifically, the shape- and size-control characteristics of surface plasmon resonance (SPR) of Au inorganic nanoparticles (NPs) have been extensively utilized in bio-tracking, chemical sensors, electronic devices, medical therapies, and imaging agents[1–15]. When the wavelength of incident light coincides with the SPR wavelengths of Au NPs, the efficiency of the local field enhancement effects of the photon-to-thermal conversion[1–4], Raman scattering[10–12], and nonlinear optical (NLO)[13–15] processes can be greatly improved for theranostics. By considering scattering loss and pigment attenuation in photomedicines, recent efforts indicated that the red to NIR wavelength would be a better choice for deep tissue treatment[16,17]. However, red-NIR-IR excitation wavelengths for these optical applications were still difficult to obtain despite the manipulation of isotropic Au NPs[1–4,13–15]. Various strategies[18–27] for the preparation of shape- and size-controlled Au nanomaterials have been developed. These procedures require complex experimental conditions, toxic reagents (i.e., CTAB, organic solvent, and initiator compounds), and multiple synthesis steps to obtain plasmonic Au NPs with the desired SPR band and surface functionality. Packing Au NPs into amphipathic co-polymers might prevent their aggregation under the

previously mentioned physiological conditions by sterically protecting their surfaces and allowing specific functional groups to be exposed to their subsequent conjugations. The intrinsic amphipathic features of the polymer in the inorganic-polymer hybrid can act as additional absorption sites for drug delivery. Although several reports have successfully employ amphipathic co-polymers to coat and encapsulate the nanoparticles via a step-by-step strategy through the ligand exchange and micelle formation surface strategies[28–33], these methods are still difficult to control synthesis of the nanocrystal core sizes and types accompanying with synchronous self-assembly of co-polymer on the particle surface.

In this study, we first focused on devising a novel green method (water system) which enables us to synthesize size-tunable Au NPs and form Au@polymer nanostructures via a spontaneous redox reaction between a $HAuCl_4$ precursor and the amphiphilic block copolymer poly(styrene-*alt*-maleic acid) (PSMA) (Figure 1a). Only two reagents were employed and controlling the reaction time enabled the analogical layer-by-layer growth of the PSMA polymer on the Au NPs (Au@PSMA polymer, abbreviated as Au@polymer) through polymer self-assembly and esterification. Intriguingly, the attached polymer layer was degradable by adding esterase or adjusting to basic conditions. We established a red-shifted SPR absorption of the Au@polymer structure by an increase in the polymer thickness thereby enhancing the NLO multiphoton fluorescence by excitation at 1250 nm infrared light. The surface of the Au@polymer NPs consisted of hydrophobic polystyrene blocks that could adsorb a large amount of aromatic drugs (i.e., doxorubicin (DOX), methylene blue (MB), and chlorin e6 (Ce6)) via π-π stacking interactions. We demonstrated that the Au@polymer NP carrier of the MB photosensitizer exhibited shell-dependent, surface-enhanced Raman scattering (SERS) properties. Putting these properties together (Figure 1b), the MB-loaded Au@polymer exhibited SERS and an intrinsic NLO fluorescence, allowing the observation of the distribution of MB molecules delivered to the cell.

PSMA is an inexpensive, commercially available copolymer that has been employed in the synthesis of hydrophobic nanocrystals with carboxylate functional groups in aqueous solutions[32–34]. Recent studies showed that PSMA micelle composites can serve as nanocarriers due to hydrophobic interactions between the styrene moiety and the anticancer drug[35,36]. Thus, the use of PSMA polymer is suitable for the development of different nanoobjects. In addition to preparin Au@polymer NPs, we further demonstrated that the polymer-assisted synthesis strategy provides a general, one-pot reaction to prepare other inorganic-organic NPs (Figure 1c), such as metal@polymer and metal oxide@polymer NPs.

Results

In a typical Au NP synthesis, 10 mL of the PSMA polymer (6 mg/mL) was reacted with 0.25, 0.5, and 1 mL of an $HAuCl_4$ (5 mM) solution at 200°C for 1 h to produce NPs with diameters of ~15 nm, ~19 nm, and ~22 nm, respectively (Figure 2a–c). The particle size was analyzed with transmission electron microscopy (TEM). With the increase of particle size from ~15 nm to ~22 nm, the absorption band of Au NPs shows little red-shift (Figure 2d). The changes of particle diameters and absorption peaks as a function of $HAuCl_4$ concentrations were summarized in Table S1.

Notably, in a high-magnification TEM image (Figure 3a), a thin coating (with low contrast) was observed on the Au NPs (1 h), suggesting that a condensed polymer nanolayer was generated. Au NPs with a diameter of 22 nm were used to study the effect of the reaction time on the polymer deposition because their larger particle size facilitated their observation. Time-dependent TEM images (Figure 3a–c) determined that the polymer shell coating became thicker and the diameter of the Au NPs was almost constant (22–23 nm) yet as the reaction time increased. At 13 h, the structure is similar to stuffed tapioca nanoball. Accordingly, along with an increase in the polymer thickness, the local SPR extinction signal showed the expected bathochromic shift (Figure 3d). It would be ascribed to a change in the proximal environment affecting the dielectric constant of the surrounding media[30,31]. At the same time, a broader absorption tail extending into the visible region accompanied by a shoulder at 260–300 nm appeared after reaction for 10 h and 13 h. The evolution of the new absorption feature could be associated with the generation of carbonyl groups and/or an increase in the number of conjugated double bonds in the condensed polymer structure[37,38]. These results are summarized in Table S2 and Figure 3e.

We further employed a Raman spectrometer (Figure 3g) to characterize the Au@polymer nanocomposite structure. Although most of the peaks in Au@polymer NPs are inconsistent with these in free PSMA polymer, the vibration signals appeared for samples at 1–6 h of reaction time indicated the organic materials has been deposited on the Au NPs because only $HAuCl_4$, H_2O, and PSMA polymer were reacted. The Raman spectra of the Au@polymer NPs at 13 h showed two broaden bands at 1584 cm^{-1} and 1330 cm^{-1}. This observation has suggested that for the PSMA polymer converting to more condensed carbon structures[39] (e.g., amorphous graphite or polycyclic aromatic hydrocarbons). However, the products at 13 h was subjected to analysis by using the synchrotron X-ray powder diffraction pattern (Figure 3f) to prove the formation of the Au@polymer nanostructure. The sharp peaks of the face-centered-cubic structure of Au

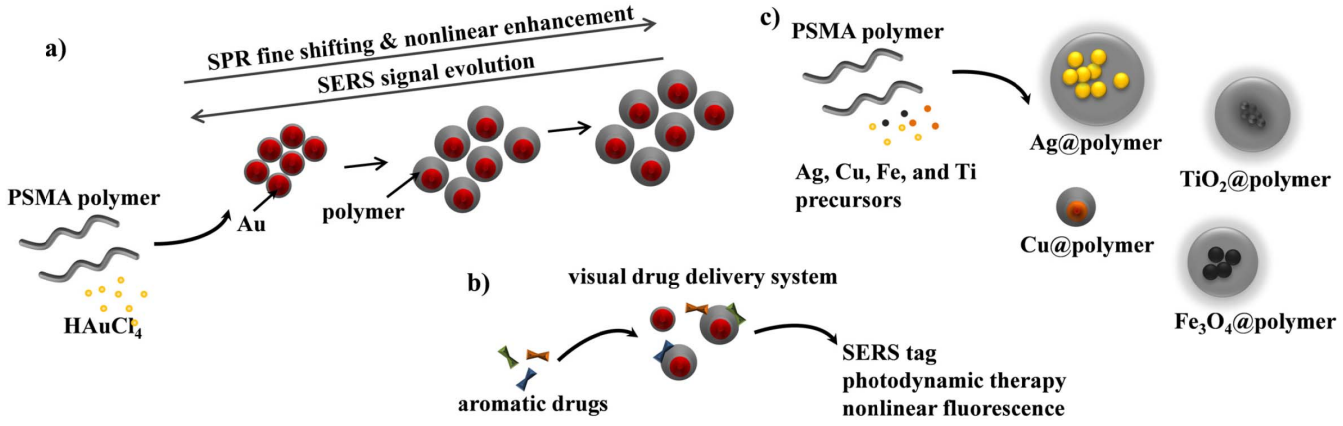

Figure 1 | Schemes illustrated the polymer-assisted reduction of the $HAuCl_4$ precursor to prepare Au@polymer NPs a), which exhibited polymer shell-dependent SERS and nonlinear optical enhancements for the observation of microscopic drug delivery in system b). c) The synthesis strategy using the different metal salt precursors to prepare Ag@polymer, Cu@polymer, TiO_2@polymer, and Fe_3O_4@polymer NPs.

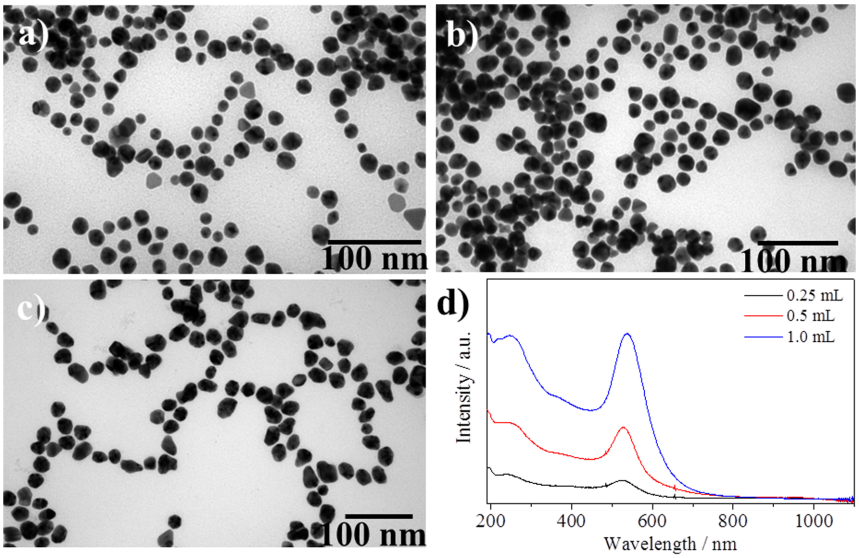

Figure 2 | TEM images of the Au NPs prepared by the reaction of 0.25-mL a), 0.5-mL b), and 1-mL c) $HAuCl_4$ (5 mM) with 10 mL of PSMA polymer (0.78 mg/mL) at 200°C for 1 h. d) UV-visible spectra for these corresponding Au NPs.

(JCPDS No. 89-3697) appeared. Additionally, it exhibited a broadening band at ~14° that could be ascribed to the generation of condensed organic composites.

To validate the growth of the PSMA polymer on the Au NPs, we recorded the FT-IR spectra to monitor the changes in the surface structure during the reaction (Figure S1). Note that among these IR peaks, the bands at 1720–1760 cm^{-1} were owing to the overlapping of C = O groups in carboxylic acids, carbonyl moieties, and ester bonds which became to rise in the intensity for the resultant Au@polymer NPs after 10–13 h. To verify the formation of the ester bonds in the inorganic-organic nanocomposites, TEM images observed that the reaction with the esterase caused the dissociation of the polymer shell structures, suggesting that the polymer sheath could be biodegradable (Figure S2). The zeta potentials measured for the as-prepared Au@polymer NPs (at pH = 6.4) at 1 h and 13 h were −18.6 mV and −42.1 mV, respectively, whose magnitude is increased as the polymer shell getting thicker. Indeed, the presence of electrostatic potential on the particle surface was also verified by attracting inorganic Fe_3O_4@CTAB and amine-functionalized QDs onto the negatively charged Au@polymer NPs (Figure S3). These results confirmed the numerous carboxylate groups exposed to the outmost surface of Au NPs.

Previous reports indicated that the thermal reaction of a $HAuCl_4$ solution with a carboxylate ligand (e.g., citrate molecule) yielded Au

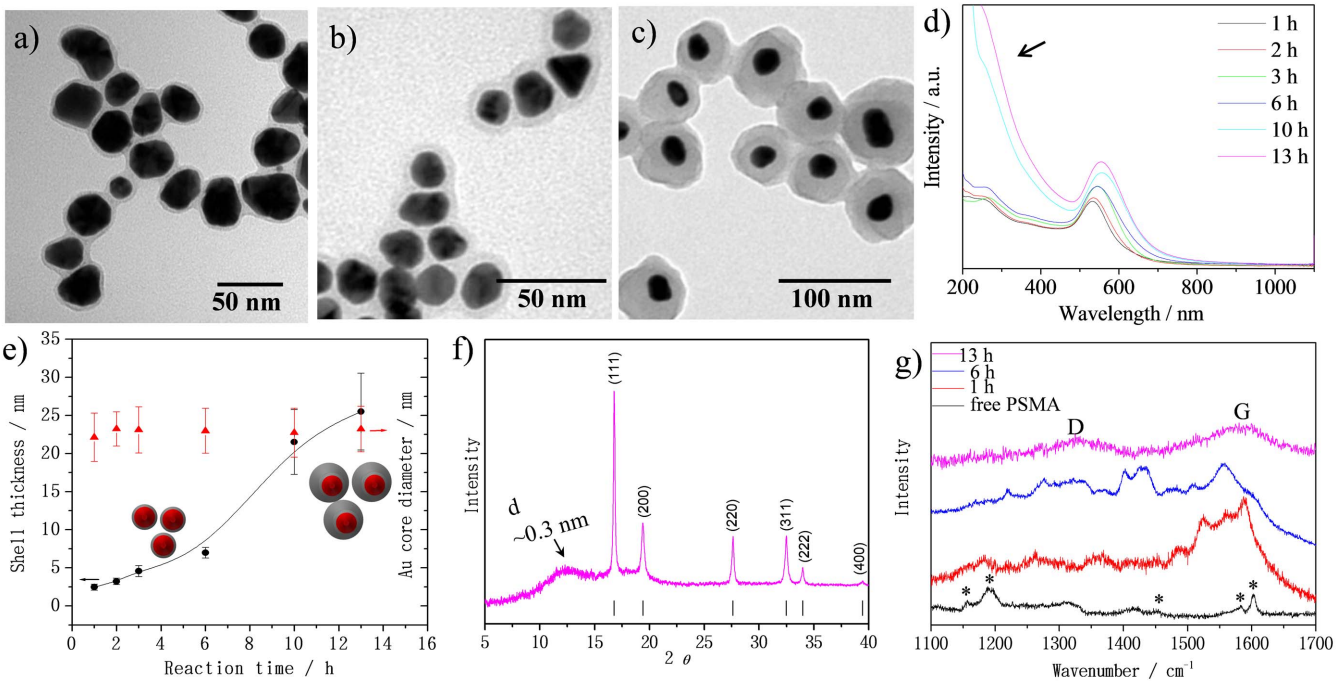

Figure 3 | Time-dependent examinations of the a-c) TEM images from 1 h to 6 h to 13 h and d) UV-visible absorption spectra for the as-prepared Au@polymer NPs (~22 nm in core size). e) Au core size/polymer shell thickness plots f) Synchrotron X-ray powder diffraction pattern of the 13 h sample of the Au@polymer NPs. g) Raman spectra of the 1, 6, and 13 h samples of the Au@polymer NPs, where the * symbol shows the styrene portion of PSMA and the D/G bands refer to the sp^3/sp^2 hybridized carbon atoms of the graphite structure.

colloids because of the electron donation from the oxidizing COOH groups and the release of CO_2 molecules[40]. To study the reducing ability of the PMSA polymer, we reacted different concentrations of the PSMA polymer (60–300 μg/mL) with 1 mL of 5 mM $HAuCl_4$ (Figure S4). A peak at approximately 303 nm appeared during the 1 h thermal reaction with 60–150 mg/mL of PSMA, which is consistent with the UV-visible results. This band originated from the formation of a complex with Au(III) ions[41]. The complete reduction of 5 mM $HAuCl_4$ required at least 300 μg/mL of the PSMA polymer. Additional experiments in which the PSMA polymer was replaced with malic acid and succinic acid as Au^{3+} reducing agents were performed (Figure S5). Micron-sized Au particles were produced from the reduction of the Au^{3+} ions. As the same reaction with the PSMA polymer analogues (i.e., poly(4-styrenesulfonic acid-co-maleic acid) sodium salt and poly(maleic anhydrate-alt-1-octadence)), the formation of a colloidal Au solution was detected with TEM and UV-visible spectroscopy (Figure S6). These results indicated that the PSMA carboxylate groups contributed to the Au reduction, while the polymer structure controlled the particle size through steric interactions. We deduced that the continuous polymer self-assembly on the Au NPs due to the increase in the internal hydrophobicity via π-π stacking interaction between polystyrene blocks of PSMA structure[29–36].

Then we demonstrated the optical enhancements in the NLO and Raman scattering signals of this new Au-polymer nanostructures. We measured the multiphoton spectra of all single-domain Au@polymer NPs (2–13 h) with a 30 s integration time by exciting them with a 1250 nm femtosecond laser (~100 fs) (Figure 4a). Narrow peaks at 625 nm and 416 nm was assigned to the generation of second harmonic generation (SHG) and third harmonic generation (THG) signals, respectively, because of their triple and double frequency of the fundamental excitation at 1250 nm[17]. The origin of the two-photon excitation and three-photon excitation processes was verified according to the pump-power dependence examinations (Figure S7), which gave the slopes of 2.05 for the SHG signal and 2.9 for the THG signal. It could be the system noise that deviate the results a little bit from ideal dependency. Note that a broad emission band at ~685 nm was raised with the increase of polymer thickness on the Au NPs. It displayed a near squared dependence (~1.7) of yields on the excitation power (Figure S7), suggesting that the broad fluorescence might be coming from the two-photon fluorescence (TPF). The TPF intensity of the Au@polymer NPs at 13 h was approximately 37 times greater than that of the product at 2 h. Since the Au@polyme NPs at 13 h have increased absorption intensity at 600–650 nm, we attribute the enhancement of TPF to the two-photon resonant excitation by 1250 nm laser pulses. As a double check, we added NaOH solution in it (Figure S8). The corresponding TPF intensity of the 13 h sample was remarkably suppressed and accompanied by a blue shift of SPR absorption (Figure S8c). Notably, the TEM image (Figure S8b) revealed the dissociation of the surface-condensed organic coating from the structures, which might be caused by the deprotonation of residual COOH groups and the strong breaking of ester bonds. Although the detailed mechanism involved in the increased TPF intensity of Au@polymer NPs is not clear, it could be the aggregation of Au NPs that resulted in inter-particle coupling, red-shift of SPR band, and enhancement of TPF[13,14,42,43].

To investigate the Raman scattering performance, the SERS signal of MB molecules on the single-domain Au@polymer NPs was measured (with a 633 nm laser excitation at 17 mW for 1 s) (Figure 4b). The MB photosensitizer was chosen as a model drug for the SERS tag because of its good resonance action by exciting at 633–660 nm. The absorptive amount of MB molecules on the Au@polymer NPs was estimated to be 0.078 mg/$mg_{[Au]}$ for the 1 h sample and 0.12 mg/$mg_{[Au]}$ for the 13 h sample on the basis of the UV-visible measurements. Compared with pure MB, the enhancement factors of the 1623 cm^{-1} peak were approximately 3.7×10^4 (1 h), 1.3×10^4 (2 h), and 2.5×10^3 (6 h). The 13 h sample did not exhibit the characteristic Raman peaks of MB molecules. A similar trend in the shell-dependent Raman signal enhancement was observed (Figure S9) by using a 785 nm NIR laser (80 mW and 5 s). Because thinner polymer coatings resulted in smaller gaps between the spatially isolated Au nanoparticles, we proposed two possible mechanisms for the shell-dependent SERS signals of the Au@polymer NPs substrate. The first involved the SERS signal from the ensemble average of each isolated Au@polymer-MB NP. The MB molecules in the polymer sheath were very close to the outermost edge of each Au core (~2.46 nm or less), which is similar to the isolate particle-based enhanced Raman effect[44]. Second, only the MB molecules were in close proximity to the discrete Au NPs, which would increase the resonance associated with the strong Raman vibration[45].

In addition to encapsulating positively charged MB dye, we found that the Au@polymer NPs (6 h-sample as example) could successfully encapsulate negatively charged Ce6 and positively charged DOX molecules (Figure 5). The absorption of MB, Ce6, and DOX in the Au@polyme NPs was saturated at 0.10 $mg_{[MB]}/mg_{[Au]}$, 0.34 $mg_{[Ce6]}/mg_{[Au]}$, and 0.73 $mg_{[DOX]}/mg_{[Au]}$, respectively. TEM images revealed that the polymer sheath contrast on the Au NPs increased and became dark gray after the absorption of these aro-

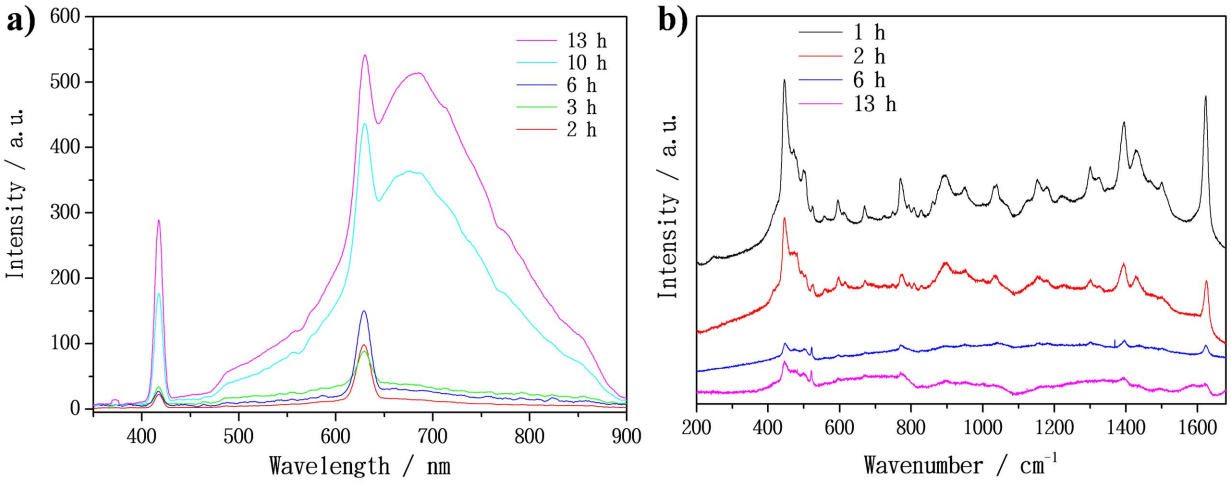

Figure 4 | a) Nonlinear optical spectra of the as-prepared Au@polymer NPs at different reaction times and b) Raman shift detection of MB-tagged Au@polymer NPs (prepared over 1–13 h) at an excitation of 632.8 nm.

matic molecules (Figure S10). The change in the images strongly suggested that the aromatic drugs were absorbed within the Au@polymer nanocarriers. The peaks of each molecule appeared in the UV-visible and fluorescence spectra of the Au@polymer nanocarriers (Figure 5). The emission intensities of the molecules in the Au@polymer-dye nanocomposites were smaller than those of the individual molecules at the same concentration, suggesting a quenching effect of the Au core interior. Especially, the Ce6-loaded particles had a good fluorescence signal (IVIS® Spectrum), which was suitable for fluorescent imaging in vivo (Figure S11). Our result showed that the payload of the aromatic drugs in the Au@polymer NPs is independent of the charge on the molecule.

However, it is worth to note that the 1 h sample of MB-tagged Au@polymer NPs exhibited strong SERS signals (black curve in Figure 4b). MB molecule is known that 660 nm NIR light is able to induce $^1O_2$ photogenerated source ~0.5 of quantum yield, and it therefore has potential for application in photodynamic therapy[46,47]. The delivery of Au@polymer-MB NPs to HeLa cervical cancer cells was therefore examined using the 1 h sample. As shown in Figure 6a, the MTT assay showed that the Au@polymer-MB NPs did not have significant cell toxicity up to 20 μM of MB molecules. Free MB molecules (0–20 μM) were also used for comparison and had toxic effects (dark toxicity) on the cells between 10 and 20 μM. We performed a parallel experiment to monitor the release of MB from the Au@polymer-MB NPs in a PBS solution at 37°C (Figure S12). The UV-visible optical record shows that their release (<8%) into solution at pH = 7.4 was limited. The release only obtained under a base condition. In vitro test supports that the π-π interactions between the MB molecules and the polymer sheath of the Au@polymer NPs might inhibit the release of MB via a diffusion pathway. The MB molecules did not leak significantly from the Au@polymer NPs, which would prevent the formation of lesions on the mitochondria and nuclei[47].

For the particle-treated cells at 24 h, the accumulation of MB-loaded carriers in the cell body of the HeLa cells was easily confirmed by a SERS microscopy. With a bright-field microscopy (Figure 6b), two individual cells were randomly selected in the rectangle (Figure 6b, red rectangle) for SERS analysis of the signal intensity at 1623 cm^{-1}. The reconstructed SERS imaging with the magenta color contrasts showed that the signal was absent in the nuclei region, in agreement with the keep of MB on the Au@polymer nanocarriers. By using nonlinear optical microscopy, we could directly observe the delivery of the Au@polymer nanocarriers into the cell by monitoring the SHG and THG emissions with high contrast and low background autofluorescence (Figure S13). Nuclei of cells can be clearly identified with negative contrast in the image. Because cells wouldn't have strong SHG signals or two-photon autofluorescence excited at 1250 nm, these NLO signals certainly came from nanocarriers taken up by cells. The NLO images also indicated that the internalized Au@polymer-MB NPs were located in the cytoplasm of the cells rather than in the nuclei, which is consistent with the SERS imaging results.

Next, we utilized fluorogenic substrate 2′,7′-dichlorodihydrofluorescein diacetate (DCFH-DA), a cell-permeable dye, for detection of singlet oxygen in cells. In this method, colorless DCFH-DA molecules crosses cell membranes react with reactive oxygen species to produce green fluorescent DCF. All DCFH-DA stained cells were incubated with samples and illuminate with 660 nm light. Brighter green fluorescence was detected in Au@polymer-MB NPs treatment group more than that by free MB under same drug concentration (Figure 6c and 6d). The level of intracellular ROS presented as an

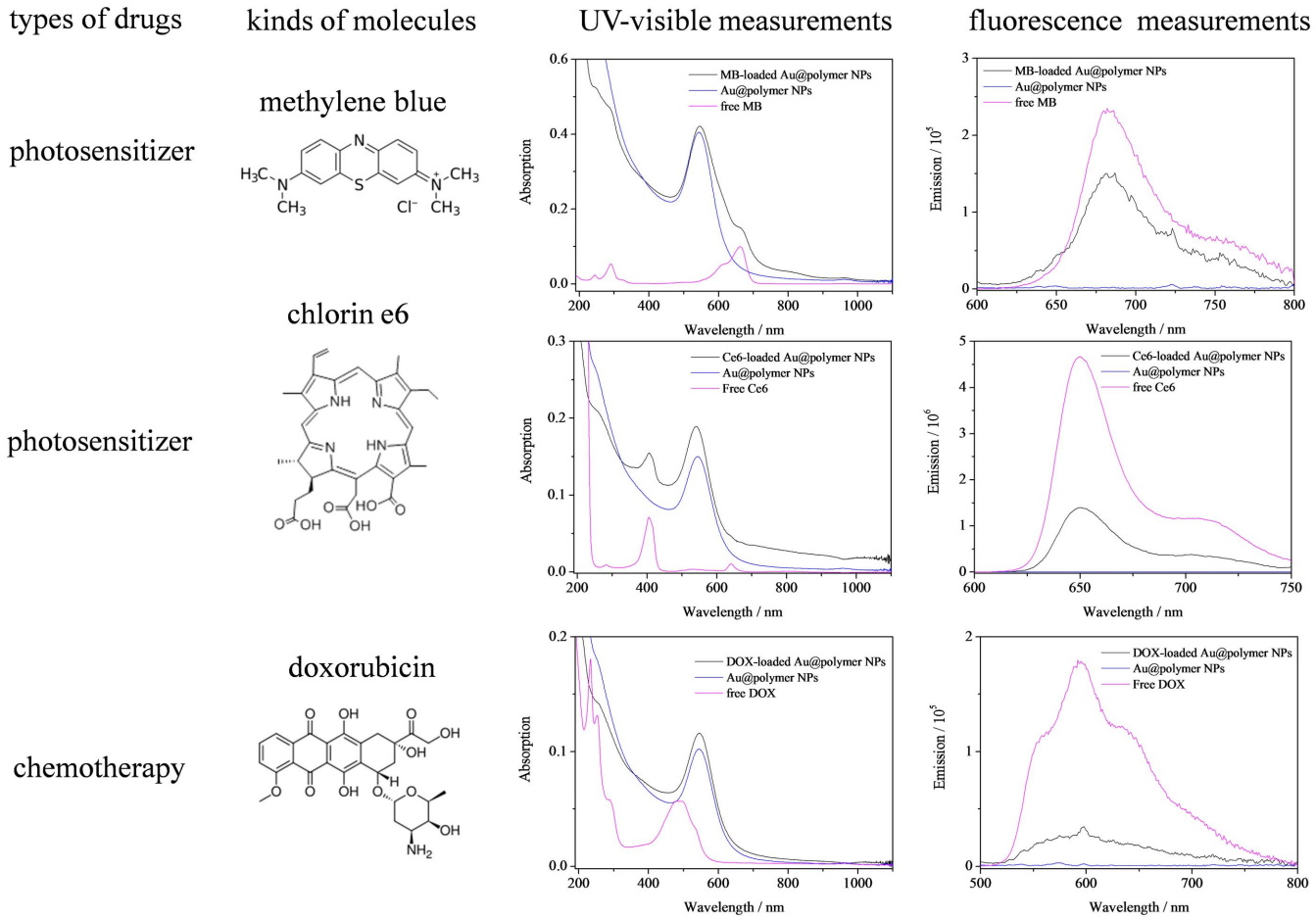

Figure 5 | UV-visible and fluorescence spectra of different aromatic drugs encapsulated in the Au@polymer NPs (6 h-sample).

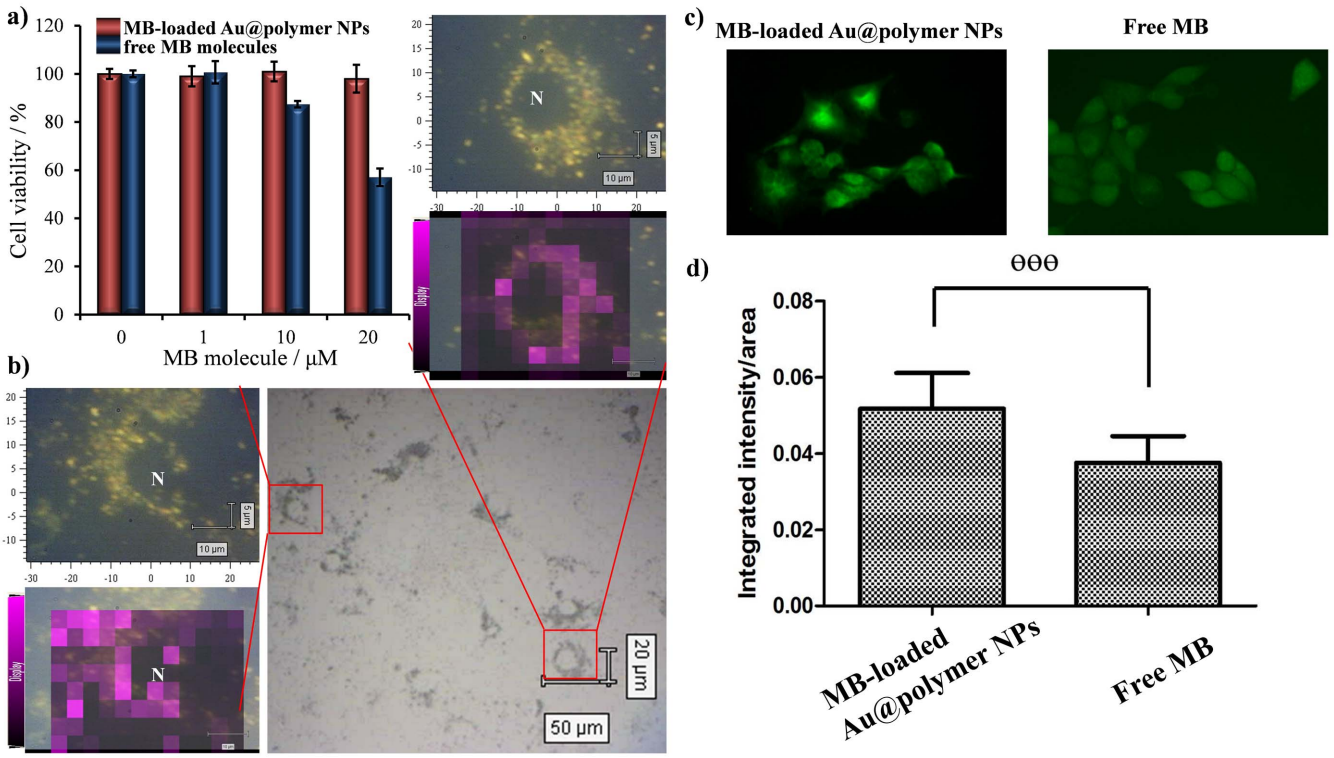

Figure 6 | a) MTT assay of HeLa cells with free MB molecules and MB-loaded Au@polymer NPs at 24 h. b) Bright-field image of the HeLa cells with MB-loaded Au@polymer NPs and two SERS mapping images (based on the 1623 cm^{-1} vibration of MB) collected for the rectangle shown in the bright field of a HeLa cell. N indicates the nucleus. c) Fluorescence images of DCFH-DA staining in HeLa cells incubated with MB-loaded Au@polymer NPs and free MB for 4 h. The sample-treated cells were exposed to LED light at 660 nm (30 mW/cm^2) for 4 min before imaging detection. d) Fluorescence intensity of MB-loaded Au@polymer NPs and free MB in HeLa cells.

important indicator for PDT. Our preliminary results showed that the Au@polymer-MB NPs could promote intracellular generation of reactive oxygen species in photodynamic therapy.

Finally, we demonstrated that this polymer-assisted synthesis method is generic allows ones to develop new conceptually designed inorganic-organic nanocomposites (Figure 1), i.e., polymer-coated Ag, Cu, Fe_3O_4, and TiO_2 NPs. In these preparations, the synthesis of these metal and metal oxide NPs required the appropriate reaction modifications through addition of N_2H_4 as a reductant and HCl in optimizing the experimental parameters to prepare highly uniform and stable NPs (Figure 7a–d). XRD measurements (Figure 7e) revealed that the samples in Figure 7a–d were face-centered cubic (fcc) Ag, fcc Cu, fcc Fe_3O_4, and anatase TiO_2. UV-visible spectra showed the SPR appearance of Ag@polymer and Cu@polymer NPs (Figure 7f). The DLS analysis of various samples in Figure 7a–d was performed and listed in Table S4. Most of the particle hydrodynamic diameters are slightly larger to their corresponded solid forms estimated based on the TEM measurements of Ag@polymer (~262 nm), Cu@polymer (~49 nm), and Fe_3O_4@polymer (~38 nm). The hydrodynamic diameter of TiO_2@polymer NPs is larger than the single particle estimation of TiO_2@polymer NPs (~84 nm) determined by TEM image, indicating the aggregates in the solution. These core-shell NPs all present negatively charged surface over −20 mV.

The comparative experiments for details and explanation can be found in Supporting Information and Figure S14–S19. As PSMA polymer alone react with $AgNO_3$, $CuCl_2$, $FeCl_2$, and titanium(IV) isopropoxide precursors, the reducing ability of PSMA polymer could only react with Ag and form Ag@polymer single-particle. We found that the reduction reaction with N_2H_4 promoted the formation of plasmonic Cu NPs (Figure S16a) as well as the assistance in the crystallization of Fe_3O_4 (Figure 7e and S17) and TiO_2 (Figure S19) particles under base condition. These reactions are done in acid-free conditions. The hydrolyzed N_22H_4 known as a reductant donates electrons accompanied with the release of OH- ions into water to precipitate metal oxides via the base-catalyzed reaction[48]. However, the interesting morphologies of multicore@polymer structure were observed for the Ag (~22 nm for each domain) after a reaction including 12 μL HCl and 100 μL N_2H_4, as shown in Figure 7a. The formation of the multicore Ag@polymer NPs resulted in a red-shift of the SPR bands at 448 nm and 545 nm. The coupling of several Ag NPs in a polymer sphere resulted in a red-shift of the SPR bands relative to those of the single Ag NPs (20 nm at 400 nm to 60 nm at 455 nm)[49]. Intriguingly, we found that the multicore Ag@polymer NPs could be dissociated by reacting with the esterase to break the ester bond linkage (Figure S2c). As the reaction of $CuCl_2$, PSMA, and N_2H_4 added with 18 μL HCl, a single sharp SPR band appeared for the Cu@polymer NPs at 590 nm (Figure 7f) in contrast to the broad band from the acid-free condition (Figure S16d).

We performed a time-dependent TEM images to monitor the growth process of multi-core Ag@polymer NPs (Figure S15). We observed a homogenous particle growth through a progressive aggregation of Ag embryos at the polymer shell as the reaction time goes. The step-by-step self-assembly of Ag NPs and polymer shell was proposed. In addition, we observed that by adding more acid favored the growth of bigger size polymer particle which resulted in more Ag/AgCl NPs encapsulated in large amount in N_2H_4-free (Figure S14b,c) method. Similarly, several TiO_2 sub-NPs aggregated into rice- and rod-shape (with 18 μL HCl and 100 μL N_2H_4) within a thick polymer matrix (Figure 7d), while the large particle size coated with thin polymer layer appeared after acid-free synthesis (Figure S19a). The adjustment of acid concentration readily played a vital role to grow bigger polymer size and include large amount of NPs. Note that the interior of Fe_3O_4@polymer (with 100 μL N_2H_4)

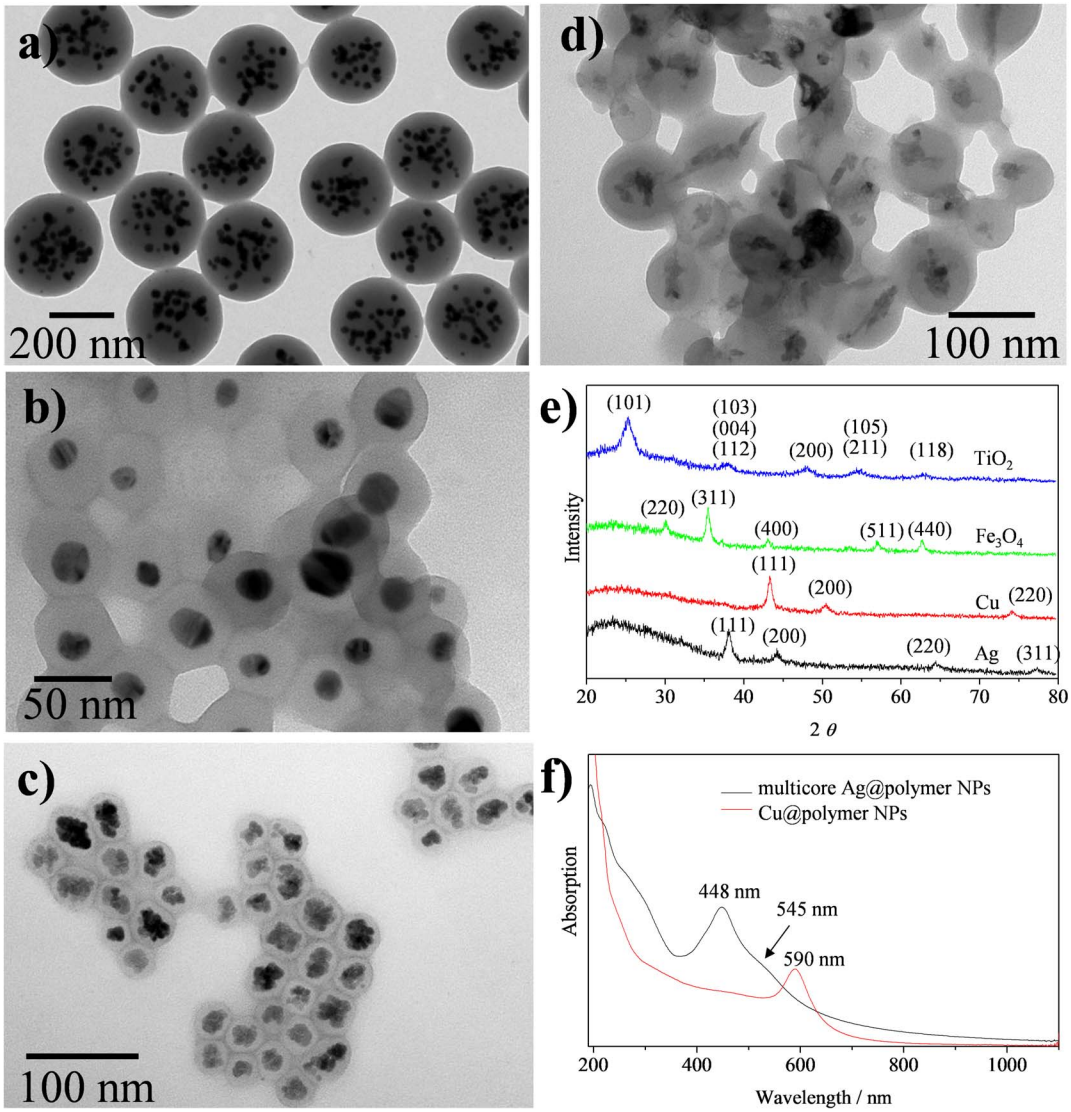

Figure 7 | TEM images of a) Ag@polymer (with 12 μL HCl and 100 μL N_2H_4), b) Cu@polymer (with 18 μL HCl and 100 μL N_2H_4), c) Fe_3O_4@polymer (with 100 μL N_2H_4), and d) TiO_2@polymer (with 18 μL HCl and 100 μL N_2H_4) NPs. e) XRD measurements for these inorganic-polymer nanocomposites going from a) the bottom to d) the top. The peaks for a), b), c), and d) were assigned based on the standard patterns of Ag (JCPDS 04-0783), Cu (JCPDS 85-1326), Fe_3O_4 (JCPDS 19-629), and TiO_2 (JCPDS 89-4921), respectively. f) UV-visible spectra of Ag@polymer and Cu@polymer NPs.

contained several nanoparticles with ~8 nm for each domain size (Figure 7c). Time-dependent TEM images (Figure S18) gave evidence of Fe_3O_4 core consisted of many small nanocrystals after 2 h of reaction time, indicating that the growth of multi-core Fe_3O_4 NP possibly followed by a clustering interaction through magnetic dipole attractions and forms a single Fe_3O_4 NP. Subsequently, the polymer shell started to grow thicker as the reaction time increase.

The multicore Fe_3O_4@polymer NPs exhibited a superparamagnetic behavior (Figure S20a), most likely due to the small domain size. We demonstrated a typical Fenton reaction toward H_2O_2 decomposition using Fe_3O_4@polymer NPs which gave great peroxidase-like catalytic activity than that by using commercial Fe_3O_4 NPs (Figure S20b). The detection in the decomposition of H_2O_2 molecule is accessible by eyes below 6 min. Also, we suggested that the highly dispersed, biocompatible, and magnetic behaviors make these Fe_3O_4 nano-clusters promising for safe use of MR contrast agent[28]. On the other hand, the multicore TiO_2@polymer NP performed good photo-catalytic degradation of MB (as an organic pollutant test) with a 0.053 min^{-1} of reaction rate constant, following with first-order reaction kinetics, under ultraviolet irradiation (8 W) at 302 nm (Figure S21). The reaction rate constant is greater than those in the literature[50]. Several TiO_2 NPs together in the polymer sphere might enhance the photodegradation.

Discussion

Au@polymer nanocomposites with a tunable Au core size and organic shell thickness were successfully synthesized via a one-pot reaction of $HAuCl_4$ and PSMA precursors. The formation mechanism was based on the crystallization of the Au NPs followed by the subsequent self-assembly and condensation of the PSMA polymer on the surface after the redox reaction. The coating polymer corona could be degraded by reaction with esterase or under basic conditions. Altering the Au-polymer core-shell structures affected the optical properties of the Au NPs. Thicker polymer coatings resulted in a red-shift in the absorption band and thus resonantly enhanced the two-photon emission at an excitation of 1250 nm. A large SERS signal resulted from a thin coating on the Au@polymer NPs because of the close proximity of the molecule to the Au surface. We demonstrated that amphipathic PSMA-coated Au NPs were very

stable under physiological conditions and therefore could deliver a high dosage of aromatic drugs and be used as an optically enhanced SERS/NLO contrast in cells. The MB-loaded Au@polymer NPs readily promoted reactive oxygen species generation into cancerous cells to execute efficiency photodynamic therapy. The self-assembly of PSMA in this synthesis strategy could be employed to prepare other inorganic@polymer NPs with appropriate addition of N_2H_4 and HCl reagents to prepare uniform and stable NPs. They showed promise for applying for new drug delivery systems in future with magnetically guided function and as an aromatic absorber following by catalytic decomposition.

Citrate ligand-assisted synthesis is a well-established method to generate Au nanoparticles with spherical shape, but it suffers from less colloidal stability under physiological conditions necessary for good biocompatibility and enhanced drug loading. Compared to the popular Turkevich's method[18,19,40] based on the thermal reduction of aurate ions ($AuCl_4^-$) with citrate molecules, the hydrodynamic diameter of as-synthesized Au@polymer NPs were very stable against aggregation in the PBS solution by using the dynamic light scattering measurements, while the citrate-capped Au NPs were not (Figure S22). This may be ascribed to the complete surface protection and strong electrostatic repulsion as Au@silica NPs. In a comparison with most popular Au@silic NPs[51,52], both of the soft polymer- and hard silica-shell composites increased the suspension stability of the Au NPs as well as chemically and physically inert surface available. To operate optical changes, we observed that PSMA polymer coatings readily modulate the red-shifting position of the surface plasmon absorbance with an increase in the polymer thickness, which is similar to that by a solid silica coating[51]. In order to conjugate biomolecules, PSMA polymer-coated inorganic NPs were facile for a directly surface modification treatment to conjugate amine terminal group of the targeting objects, using an EDC/NHS coupling reaction. However, a further modification of the silica coating layer with amino-silane coupled reaction to form Au@silica@amino-silane NPs was necessary to execute the same carbodiimide chemistry with the biological molecule at carboxylate end[52].

This is the first report of a facile PSMA-assisted synthesis strategy that incorporates amphipathic functionality on the surfaces of several inorganic NPs (Figure 1). In the case of Au@polymer NPs synthesis, we demonstrated that the polymer shell thickness is easy controlled at different reaction time. This typical synthesis method showed a direct, one-pot preparation of stable polymer-encapsulated Au, Ag, Cu, Fe_3O_4, and TiO_2 NPs without resorting to complicated surface engineering designs and synthesis parameters. Previous study of polyelectrolyte modification appeared the shortcoming of time-consuming and reagent-wasting because a repeat treatment via oppositely charged polymer attachment and purification required at each coating step[31]. In addition, the generation of thick polymer coating with the evaporation of organic solvent for polymeric micell formation[28] and cross-linked block copolymers after ligand exchange process[29] can be neglected in our one-pot synthesis reaction. Decrease usage of toxic agents involve also means more environmental green. The aforementioned reaction at the particle surface may also cause particle aggregation and was difficult to control polymer shell thickness.

Our ongoing work is investigating the new concept of PSMA polymer-based reaction to develop shape-control synthesis of Au nanoplate@polymer and Au nano-octahedron@polymer NPs for tuning the SPR band from visible to NIR wavelength. This will enable investigators to exploit *in situ* synthesis of shape-control Au@polymer NPs in new ways. The aforementioned surface coating strategies by post-synthetic strategies merely kept particle size and shape of the original ones. The same polymer-assisted synthesis also presented a facile manner to combine optical and magnetic properties by incorporating the Au NPs and Fe_3O_4 NPs together into the polymer sphere, being for a multimodal imaging agent for MRI, CT, and NOL.

Methods

Materials. Poly(styrene-*alt*-maleic acid)sodium salt, 13 wt. % solution in water (PSMA, M_w = 350000) (Sigma-Aldrich), poly(4-styrene sulfonic acid-co-maleic acid) sodium salt (M_w = 20000) (Aldrich), poly(maleic anhydrate-alt-1-octadence) (M_w = 30000–50000) (Aldrich), succinic acid (Sigma), maleic acid (99.5%) (Chem Service), quantum dot (Life), hydrogen tetrachloroaurate(III) trihydrate ($HAuCl_4$, 99.99%) (Alfa Aesar), Silver nitrate ($AgNO_3$) (Fisher), Copper(II) chloride dihydrate ($CuCl_2{\cdot}2H_2O$) (Riedel-de Haen), Iron(II) chloride tetradhydrate ($FeCl_2{\cdot}4H_2O$) (J. T. Baker), Hydrazine monohydrate ($N_2H_4{\cdot}H_2O$, 98%) (Alfa Aesar), titanium(IV) isopropoxide (97%) (Sigma-Aldrich), tetraethyl orthosilicate (TEOS, 98%) (Sigma-Aldrich), sodium hydroxide (NaOH, min 99%) (Fullin), methylene blue (MB, high purity) (Alfa Aesar), Chlorin e6 (Ce6) (Frontier), doxorubicin hydrochloride (DOX) (Sigma-Aldrich), esterase (Sigma), 3,3′,5,5′-Tetramethylbenzidine (TMB, ≥99%) (Sigma-Aldrich) were purchased for use without purification.

Preparation of Au@polymer nanoparticles (NPs). 1 mL of a $HAuCl_4$ solution (5 mM) was mixed with 10 mL of a PSMA solution (6 mg/mL) under stirring, and then the mixture solution was immediately transferred to a 23 mL Teflon-lined stainless steel autoclave and heated at 200°C. After different reaction times (1–13 h), the as-prepared Au@polymer NPs were collected by centrifugation and washed with distilled deionized water. To prepare the Au@polymer NPs with core size tunable, 0.25–1.0 mL of an $HAuCl_4Cl$ solution (5 mM) was added to the PSMA solution (6 mg/mL) before the hydrothermal reaction. Once these reagents were mixed, the resulting solution was transferred to a 23 mL Teflon-lined stainless steel autoclave and heated at 200°C for 1 h. These Au@polymer NPs were purified using the aforementioned method of centrifugation and redispersion in water.

10 mM of an NaOH solution or 2 ppm of esterase was utilized to degrade the polymer structure of the Au@polymer NPs by a direct mixture reaction after 24 h.

Preparation of Ag@polymer, Cu@polymer, Fe_3O_4@polymer, and TiO_2@polymer NPs. To prepare Ag@polymer, Cu@polymer, and TiO_2@polymer NPs, a store aqueous solution including $AgNO_3$ (5 mM), $CuCl_2$ aqueous solution (5 mM), and titanium isopropoxide (10 wt% in ethnaol) were respective preparation before reaction. 1 mL of the metal chloride solution precursors and 5 μL of titanium isopropoxide solution was subsequent reaction with 10 mL of a PSMA solution (6 mg/mL), 0.1 mL of N_2H_4, and 12–18 μL of HCl (2 M) under hydrothermal treatment at 200°C for 13 h. In the absence of HCl, a mixture of an $FeCl_2$ aqueous solution (1 mL at 5 mM), 10 mL of a PSMA solution (6 mg/mL), and 0.1 mL of N_2H_4 was employed for preparing Fe_3O_4@polymer NPs after hydrothermal reaction at 200°C for 13 h. These inorganic-polymer nanocomposites were purified using the aforementioned method of centrifugation (5000 rpm) and redispersion in water.

Absorption of Fe_3O_4 and quantum dot NPs on the Au@polymer NPs. Fe_3O_4@CTAB NPs were prepared by the thermal decomposition synthesis following by phase transformation reaction according to the literatures[33]. Qdot® 655 ITK™ amino (PEG) quantum dot (QD-655 nm) was purchase from Invitrogen for use without purification. 40 μL of Fe3O4 (100 ppm) and 40 μL of QD-655 nm (8 μM) were mixed with 200 μL of 30 ppm Au@polymer NPs (13-h sample) for 24 h to prepare Au@polymer-Fe_3O_4 and Au@polymer-QD NPs, respectively. The NPs were purified using the aforementioned method of centrifugation and redispersion in water before TEM measurements.

Encapsulation of methylene blue molecules in the Au@polymer NPs. A mixture of 1 mL of an Au@polymer NP (65 $ppm_{[Au]}$) solution and 10 μM of methylene blue (5 mM) was rotated for 18 h for MB absorption on the NPs. Afterward, the excess methylene blue was removed by centrifugation. The supernatant was examined with UV-Visible spectroscopy to record the absorbance of the solution and estimate the amount of MB absorbed on the Au@polymer NPs. The MB-loaded Au@polymer NPs were purified by a centrifugation-washing process three times and finally stored in pure H_2O before use.

Determination of the Raman Enhancement Factor of MB-loaded Au@polymer NPs. For all of the SERS measurement, an 8 μL of MB-loaded Au@polymer sample solution (~100 ppm) was deposited on the respective Si substrate by using a dip-coating method and then slowly dried under a digital controlled dry cabinet under 30–35%RH. The dry sample resulted in a sphere-shaped area of around 5.3 mm^2. Subsequently, the sample substrates were subjected to Raman spectrometer analysis.

The Raman enhancement factor of the Au@polymer-MB NPs-containing substrates was determined using the following expression,

$$EF = \left(I_{SERS}/I_{free\ MB}\right) \times \left(N_{free\ MB\ on\ the\ Si\ wafer}/N_{MB\ on\ the\ Au@polymer\ NPs\ on\ the\ Si\ wafer}\right)$$

where I_{SERS} and $I_{free\ MB}$ indicate the vibration scattering intensities in the SERS and normal Raman spectra, respectively. I_{SERS} and $I_{free\ MB}$ were calculated for the strongest peak at ~1623 cm^{-1}. $N_{MB\ on\ the\ Au@polymer\ NPs\ on\ the\ Si\ wafer}$ and $N_{free\ MB\ on\ the\ Si\ wafer}$ represent the number of MB molecules on the surface of a single Au@polymer NP and the free MB molecules deposited on the Si substrate, which excited by laser beam. The diameter of sample coating area is around 0.3 cm. The MB molecules on the Au@polymer NPs was estimated on the basis of the UV-visible measurements (e.g., 0.078 $mg_{[MB]}/mg_{[Au]}$ for 1 h-sample and 0.12 $mg_{[MB]}/mg_{[Au]}$ for 13 h-sample. In the *EF* estimation, we assume the deposition of the Au@polymer-MB NPs and free MB molecules was homogeneous on the Si wafer.

Cytotoxicity analysis. For the MTT assay, the cell treatments and preparation parameters were based on the previous literature[4]. Hela cell (5000 per well) in the 96-well plate was cultured in Dulbecco's modification of Eagle's medium plus 10% fetal bovine serum at 37°C under 5% of CO_2 in air. MB-loaded Au@polymer NPs was dispersed in the fresh medium solution. After 1 day of culture time, the culture medium in each well was then removed, and the seeding cells we separately treated with 0.1 mL of MB-loaded Au@polymer NPs medium solutions in a series of MB concentration at 0, 1, 10, and 20 μM. Through 24 h incubation, the culture medium was then removed and replaced with 100 μL of the new culture medium containing 10% MTT reagent. The cells were then incubated for 4 h at 37°C to allow the formazan dye to form. The culture medium in each well was then removed, and dimethyl sulfoxide (DMSO) (200 μL/well) was added for an additional 10 min of incubation. After the cells were centrifuged, the resulting formazan in each well was transferred to an ELISA plate. The quantification determining cell viability was performed using optical absorbance (540/650 nm) and an ELISA plate reader. In dark toxicity, the culture experiment was carefully worked under dark condition to prevent from the light exposure. Free MB molecule was also following the aforementioned processes to be the control experiment.

SERS microscopic imaging. Before cells for SERS spectral analysis, Hela cells were pre-cultured in an 8 wells of Lab-Tek™ chamber slide™ (10000 cells per well) for 2 days. After incubation, the original medium was removed and 0.3 mL of MB-loaded Au@polymer NPs (10 ppm) in the medium was added to treat with cells. Through 24 h of incubation time, the supernatant solution was carefully discarded and then the particle-treated cells on the slide are washed with PBS. Subsequently, these cells fixed using 4% paraformaldehyde/PBS for 30 min at 37 °C. The cell-containing chamber slide™ was transferred to a Renishaw inVia Raman microscope to obtain cellular images. A 68× objective lens with a working distance of 7.0 mm to collect point to point signals with computer-controlled x, y-stage in 4.0 μm that all were set up under the Raman microscope measurement. Each data point was at a 1s acquisition time. All spectral controls, manipulations, and data analysis were performed using WiRE software from Renishaw.

Nonlinear microscopic imaging. To evaluate the two-photon fluorescence contrast, the Au@polymer NPs-treated cells were studied. The imaging system is a femtosecond laser based multiphoton nonlinear optical microscope with sub-micron 3D spatial resolution[17]. The laser wavelength operates at approximately 1250 nm, which falls in the NIR penetration window (1200–1300 nm) of most biological tissues. Compared with the commonly used Ti:sapphire laser (700–1000 nm), this wavelength does not two-photon resonantly excite the soret band of many endogenous fluorophores in cells and tissues and thus, causes the least on-focus damage. Give its advantages for in vivo imaging in deep tissues, it has been widely applied in studies of developmental biology and in human clinical use. Because most autofluorescence is suppressed, the optical contrast agents that can efficiently excite at approximately 625 nm have high contrast and benefit deep tissue imaging. The laser beam was XY-scanned by a scanning unit (FV300, Olympus) cascaded with an inverted microscope (IX71, Olympus). The laser beam transmitted a multiphoton dichroic beam splitter (edged at 665 nm) and was focused using a water immersion objective (NA = 1.2, 60×, Olympus). The generated second harmonic generation (SHG) and third harmonic generation (THG) were epi-collected by the same objective. The SHG and THG signals were reflected and then separated by another dichroic beam splitter edged at 490 nm. They were detected separately by two other PMTs. All three signal channels were reconstructed to 512 × 512 images with software in computer with a 2 Hz frame rate. To image the live cells, a micro-incubator on a microscope was used to create an environment with a temperature of 37°C in an environment that was 5% CO_2/95% air. The temperature of the thermostat (LAUDA Ecoline Staredition RE 204) was set to 50°C to achieve 37°C at the distal ends of objective, but the vapor reaching the micro-incubator through the duct maintained the micro-incubator at approximately 37°C. The gas controller (OkO Lab) continuously supplied 5% CO_2, and maintained the outlet absolute pressure at 1 atm. The water immersion objective with 1.2 NA was heated by a dual temperature controller (TC-144, WARNER instrument). This made the temperature at the bottom of the dish that contacted the objective approximately 37°C.

Intracellular Reactive Oxygen Species Detection. The detection of intracellular reactive oxygen species was measured using fluorogenic substrate 2′,7′-Dichlorodihydrofluorescein diacetate (DCFH-DA). Fifty thousands of Hela cells were stained with 1 mL of DCFH-DA solution (20 μM in PBS) for 30 min in darkness. Thereafter, the cells were incubated with MB-loaded Au@polymer NPs and free MB at the same MB concentration (5 μM) in the DMEM for 2 h. To wash away the free materials, the culture plate was rinsed with PBS buffer two times, and then fresh PBS was added to each well. After 660 nm NIR light illumination (30 mW/cm^2) for 4 min, a fluorescence microscope (Nikon, Eclipse 80i) was employed to observe the green fluorescence image of cells. We used imageJ software to quantify the fluorescence intensity.

Characterization. Transmission electron microscopy (JEM-2000EX II at 80 KV) was employed to obtain a more accurate of the solid particle size estimate. The dark and gray areas of the core-shell structure in electron micrographs was calculated based on 150 particles and analyzed by using SigmaScan Pro software. 5.0. The absorption and fluorescence spectra of MB-, Ce6-, and DOX-loaded Au@polymer NPs were measured by using a UV-Vis spectrophotometer (8452A; Hewlett-Packard Company, Palo Alto, CA) and a FSP 920 fluorescence spectrophotometer (Edinburgh. Instruments, UK), respectively. IR spectra were measured using a Fourier transformation infrared spectrometer (200E; JASCO International Co., Ltd., Tokyo, Japan) by KBr plate. The Au ion concentration was quantified using an inductively coupled plasma atomic emission spectrometer (ICP-AES, JY138 Spectroanalyzer; Horiba Jobin Yvon, Inc., Edison, NJ). The zeta-potential and hydrodynamic diameter of the Au@polymer NPs dispersing in an aqueous solution and a PBS buffer solution were measured using a Zetasizer analyzer (Malvern, UK). Home-built Raman spectra of Au@polymer NPs (at an exposure time of 10 s), MB-loaded Au@polymer NPs (at an exposure time of 1 s), and free MB molecules (at an exposure time of 1 s) were obtained with a 50× objective lens using Raman microscopes equipped with a 632.8-nm air-cooled He-Ne laser (17 mW) as the exciting source. The detailed structure of the imaging system has been described elsewhere[53]. For 785-nm excitation (80 mW), a Renishaw inVia Raman microscope with a 68× objective lens was applied to analyze MB-loaded Au@polymer NPs under an integrated time of 10 s. Si was utilized as a substrate for Raman examination. Thin film X-ray Diffractometer ((Bruker AXS Gmbh, Karlsruhe, Germany) was utilized to analyze the crystallization of Ag@polymer, Cu@polyme, Fe_3O_4@polymer, and TiO_2@ polymer NPs.

The powder X-ray diffraction patterns of Au@polymer nanoparticles were measured at the BL01C2 beamline of the National Synchrotron Radiation Research Center (NSRRC) in Taiwan. The ring energy of NSRRC was operated at 1.5 GeV with a typical current of 360 mA. The wavelength of the incident X-rays was 0.6889 Å (18 keV), delivered from the superconducting wavelength-shifting magnet and a Si(111) double-crystal monochromator. The diffraction pattern was recorded with a Mar345 imaging plate detector located 332.10 mm from the sample position and an exposure duration of 5 min. The pixel size of Mar345 was 100 μm. The one-dimensional powder diffraction profile was converted using the FIT2D program with cake-type integration. The diffraction angles were calibrated based on the Bragg positions of Ag-Benhenate and Si powder (NBS640b) standards. The powder sample in solution was sealed in a glass capillary with 1.0 mm diameter. To reduce the background signal from solution, a blank experiment with pure solution in capillary was repeated at the same experimental condition. The integrated intensity was obtained after subtracting the background noise.

1. Huschka, R., Neumann, O., Barhoumi, A. & Halas, N. J. Visualizing light-triggered release of molecules inside living cells. *Nano Lett.* **10**, 4117–4122 (2010).
2. Kang, H. *et al.* Near-infrared light-responsive core–shell nanogels for targeted drug delivery. *ACS Nano* **5**, 5094–5099 (2011).
3. Doane, T. L. & Burda, C. The unique role of nanoparticles in nanomedicine: imaging, drug delivery and therapy. *Chem. Soc. Rev.* **41**, 2885–2911 (2012).
4. Jin, Y. Engineering plasmonic gold nanostructures and metamaterials for biosensing and nanomedicine. *Adv. Mater.* **24**, 5153–5165 (2012).
5. Yong, K. T. Quantum dots for biophotonics. *Theranostics* **2**, 629–630 (2012).
6. Lee, J. S., Han, M. S. & Mirkin, C. A. Colorimetric detection of mercuric ion (Hg^{2+}) in aqueous media using DNA-functionalized gold nanoparticles. *Angew. Chem. Int. Ed.* **46**, 4093–4096 (2007).
7. Nam, J. M., Thaxton, C. S. & Mirkin, C. A. Nanoparticle-based bio-bar codes for the ultrasensitive detection of proteins. *Science* **301**, 1884–1886 (2003).
8. Lim, S. *et al.* Enhancing nanoparticle-based visible detection by controlling the extent of aggregation. *Sci. Rep.* **2**, 456/1–6 (2012).
9. Storhoff, J. J. *et al.* Homogeneous detection of unamplified genomic DNA sequences based on colorimetric scatter of gold nanoparticle probes. *Nat. Biotech.* **22**, 883–887 (2004).
10. Chen, G. *et al.* Measuring ensemble-averaged surface-enhanced Raman scattering in the hotspots of colloidal nanoparticle dimers and trimers. *J. Am. Chem. Soc.* **132**, 3644–3645 (2010).
11. Chen, T. *et al.* Hotspot-induced transformation of surface-enhanced Raman scattering fingerprints. *ACS Nano* **4**, 3087–3094 (2010).
12. Lu, W. *et al.* Gold nano-popcorn-based targeted diagnosis, nanotherapy treatment, and in situ monitoring of photothermal therapy response of prostate cancer cells using surface-enhanced Raman spectroscopy. *J. Am. Chem. Soc.* **132**, 18103–18114 (2010).
13. Han, F., Guan, Z., Tan, T. S. & Xu, Q. H. Size-dependent two-photon excitation photoluminescence enhancement in coupled noble-metal nanoparticles. *ACS Appl. Mater. Interfaces* **4**, 4746–4751 (2012).
14. Guan, Z., Polavarapu, L. & Xu, Q. H. Enhanced two-photon emission in coupled metal nanoparticles induced by conjugated polymers. *Langmuir* **26**, 18020–18023 (2010).
15. Tong, L., Cobley, C. M., Chen, J., Xia, Y. & Cheng, J. X. Bright three-photon luminescence from gold/silver alloyed nanostructures for bioimaging with negligible photothermal toxicity. *Angew. Chem. Int. Ed.* **49**, 3485–3488 (2010).
16. Liao, M. Y. *et al.* Innovative ligand-assisted synthesis of NIR-activated iron oxide for cancer theranostics. *Chem. Commun.* **48**, 5319–5321 (2012).
17. Liao, M. Y. *et al.* Surface state mediated NIR two-photon fluorescence of iron oxides for nonlinear optical microscopy. *Adv. Funct. Mater.* **23**, 2044–2051 (2013).
18. Daniel, M. C. & Astruc, D. Gold nanoparticles: assembly, supramolecular chemistry, quantum-size-related properties, and applications toward biology, catalysis, and nanotechnology. *Chem. Rev.* **104**, 293–346 (2004).

19. Enusten, B. V. & Turkevich, J. Coagulation of colloidal gold. *J. Am. Chem. Soc.* **85**, 3317–3328 (1963).
20. Brust, M., Walker, M., Bethell, D., Schiffrin, D. J. & Whyman, R. J. Synthesis of thiol-derivatised gold nanoparticles in a two-phase liquid–liquid system. *J. Chem. Soc. Chem. Commun.* **7**, 801–802 (1994).
21. Sau, T. K. & Murphy, C. J. Room temperature, high-yield synthesis of multiple shapes of gold nanoparticles in aqueous solution. *J. Am. Chem. Soc.* **126**, 8648–8649 (2004).
22. Sun, Y., Mayers, B. T. & Xia, Y. Template-engaged replacement reaction: a one-step approach to the large-scale synthesis of metal nanostructures with hollow Interiors. *Nano Lett.* **2**, 481–485 (2002).
23. Metraux, G. S., Jin, R. & Mirkin, C. A. Photoinduced phase separation of gold in two-component nanoparticles. *Small* **2**, 1335–1339 (2006).
24. Chien, Y. H., Huang, C. C., Wang, S. W. & Yeh, C. S. Synthesis of nanoparticles: sunlight formation of gold nanodecahedra for ultra-sensitive lead-ion detection. *Green Chem.* **13**, 1162–1166 (2011).
25. Kim, J. *et al.* Designed fabrication of multifunctional magnetic gold nanoshells and theirapplication to magnetic resonance imaging and photothermal therapy. *Angew. Chem. Int. Ed.* **45**, 7754–7758 (2006).
26. Wang, C. & Sun, S. Facile synthesis of ultrathin and single-crystalline Au nanowires. *Chem. Asian J.* **4**, 1028–1034 (2009).
27. Pang, X., Zhao, L., Han, W., Xin, X. & Lin, Z. A. General and robust strategy for the synthesis of nearly monodisperse colloidal nanocrystals. *Nat. Nanotech.* **8**, 426–431 (2013).
28. Nasongkla, N. *et al.* Multifunctional polymeric micelles as cancer-targeted, MRI-ultrasensitive drug delivery systems. *Nano Lett.* **6** (11), 2427–2430 (2006).
29. Kim, B. S., Qiu, J. M., Wang, J. P. & Taton, T. A. Magnetomicelles: composite nanostructures from magnetic nanoparticles and cross-linked amphiphilic block copolymers. *Nano Lett.* **5**, 1987–1991 (2005).
30. Sánchez-Iglesias, A. *et al.* Hydrophobic interactions modulate self-assembly of nanoparticles. *ACS Nano* **6**, 11059–11065 (2012).
31. Gittins, D. I. & Caruso, F. Tailoring the polyelectrolyte coating of metal nanoparticles. *J. Phys. Chem. B* **105**, 6846–6852 (2001).
32. Wang, D., Li, Z. C. & Chen L. Templated synthesis of single-walled carbon nanotube and metal nanoparticle assemblies in solution. *J. Am. Chem. Soc.* **128**, 15078–15079 (2006).
33. Huang, C. C. *et al.* Size-control synthesis of structure deficient truncated octahedral $Fe_{3-\delta}O_4$ nanoparticles: high magnetization magnetites as effective hepatic contrast agents. *J. Mater. Chem.* **21**, 7472–7479 (2011).
34. Huang, C. C. *et al.* Bifunctional Gd_2O_3/C nanoshells for MR imaging and NIR therapeutic applications. *Adv. Funct. Mater.* **19**, 249–258 (2009).
35. Greisha, K., Sawab, T., Fangc, J., Akaikea, T. & Maeda, H. SMA–doxorubicin, a new polymeric micellar drug for effective targeting to solid tumours. *J. Control Release* **97**, 219–230 (2004).
36. Larson, N., Greish, K., Bauer, H., Maeda, H. & Ghandehari, H. Synthesis and evaluation of poly(styrene-*co*-maleic acid) micellar nanocarriers for the delivery of tanespimycin. *Inter. J. Pharm.* **420**, 111–117 (2011).
37. Gwuskens, G. *et al.* Photo-oxidation of polymers—I: a quantitative study of the chemical reactions resulting from irradiation of polystyrene at 253.7 nm in the presence of oxygen. *Eur. Poly. J.* **14**, 291–297 (1978).
38. Li, T., Zhou, C. & Jiang, M. UV absorption spectra of polystyrene. *Poly. Bul.* **25**, 211–216 (1991).
39. Xu, Z., Gao, H. & Guoxin, H. Solution-based synthesis and characterization of a silver nanoparticle–graphene hybrid film. *Carbon* **49**, 4731–4738 (2011).
40. Ojea-Jiménez, I., Romero, F. M., Bastús, N. G. & Puntes, V. Small gold nanoparticles synthesized with sodium citrate and heavy water: insights into the reaction mechanism. *J. Phys. Chem. C* **114**, 1800–1804 (2010).
41. Vogler, A. & Kunkely, H. Photoreactivity of gold complexes. *Coord. Chem. Rev.* **219–221**, 489–507 (2001).
42. Guan, Z. *et al.* Band-selective coupling-induced enhancement of two-photon photoluminescence in gold nanocubes and its application as turn on fluorescent probes for cysteine and glutathione. *ACS Appl. Mater. Interfaces* **4**, 5711–5716 (2012).
43. Liu, X.-L. *et al.* Solution-dispersible Au nanocube dimers with greatly enhanced two-photon luminescence and SERS. *Nanoscale* **5**, 5368–5374 (2013).
44. Li, J. F. *et al.* Shell-isolated nnanoparticle-enhanced Raman spectroscopy. *Nature* **464**, 392–395 (2010).
45. Kneipp, K., Kneipp, H., Itzkan, I., Dasari, R. R. & Feld, M. S. Ultrasensitive chemical analysis by Raman spectroscopy. *Chem. Rev.* **99**, 2957–2976 (1999).
46. Tardivoa, J. P. *et al.* Methylene blue in photodynamic therapy: from basic mechanisms to clinical applications. *Photodiagn. Photodyn. Ther.* **2**, 175–191 (2005).
47. Lu, Y. *et al.* Methylene blue-mediated photodynamic therapy induces mitochondria-dependent apoptosis in HeLa cell. *J. Cel. Biochem.* **105**, 1451–1460 (2008).
48. Wiogo,H., Lim, M., Munroe, P., Amal R. Understanding the formation of iron oxide nanoparticles with acicular structure from iron(III) chloride and hydrazine monohydrate. *Cryst. Growth Des.* **11**, 1689–1696 (2011).
49. Cheng, D., Zhou, X., Xia, H. & Chan, H. S. O. Novel method for the preparation of polymeric hollow nanospheres containing silver cores with different sizes. *Chem. Mater.* **17**, 3578–3581 (2005).
50. Peng, X. & Ichinose, I. Manganese oxyhydroxide and oxide nanofibers for high efficiency degradation of organic pollutants. *Nanotechnology* **22**, 015701(1)–(7) (2011).
51. Schulzendorf, M., Cavelius, C., Born, P., Murray, E. & Kraus, T. Biphasic synthesis of $Au@SiO_2$ core-shell particles with stepwise ligand exchange *Langmuir* **27**, 727–732 (2011).
52. Jana, N., Earhart, C. & Ying. J. Synthesis of water-soluble and functionalized nanoparticles by silica coating. *Chem. Mater.* **19**, 5074–5082 (2007).
53. Chiu, Y. *et al.* Quantitative and multicomponent analysis of prevalent urinary calculi using Raman spectroscopy. *J. Raman Spectrosc.* **43**, 992–997 (2012).

Acknowledgments

This work was supported by the Ministry of Science and Technology, Taiwan (NSC 101-2113-M-010-002-MY2, NSC 101-2627-E-010-001, NSC 102-2221-E-010 -006 -MY3, NSC 102-2221-E-002-195-MY3) and a grant from Ministry of Education, Aiming for the Top University Plan. We gratefully thank Mr. Cheng-Wei Lin for sample preparations.

Author contributions

T.M.L., J.Y. and C.C.H. proposed and designed the experiments. T.M.L., J.Y. and C.C.H. wrote the manuscript. T.M.L. and C.C.H. interpreted the results. C.C.H. carried out the synthetic experiments. C.A.C., A.C., H.K.C., C.H.W., P.A.C. performed the optical experiments and analyzed the data. Y.C.C. performed the synchrotron X-ray experiments and analyzed the data. C.H.H. performed the cell culture. All authors reviewed the manuscript.

Additional information

Supplementary information accompanies this paper at http://www.nature.com/scientificreports

Competing financial interests: The authors declare no competing financial interests.

How to cite this article: Liu, T.-M. *et al.* One-step shell polymerization of inorganic nanoparticles and their applications in SERS/nonlinear optical imaging, drug delivery, and catalysis. *Sci. Rep.* **4**, 5593; DOI:10.1038/srep05593 (2014).